

# Modeling and Electrical Characterization of CO<sub>2</sub>/Ar Dielectric Barrier Discharges at Atmospheric Pressure

Mohamed Chenoui\*, Hocine Tebani, Djilali Benyoucef

Laboratory of Electrical Engineering and Renewable Energy (LGEER), Electrical Engineering Department, Faculty of Technology, Hassiba Benbouali University of Chlef, Algeria.

Received: 23<sup>th</sup> September 2025; Revised: 21<sup>th</sup> November 2025; Accepted: 22<sup>th</sup> November 2025  
Available online: 28<sup>th</sup> November 2025; Published regularly: April 2026



## Abstract

In this study, a one-dimensional fluid model is employed to analyze the electrical and physicochemical properties of dielectric barrier discharges (DBDs) in pure CO<sub>2</sub> and CO<sub>2</sub>/Ar mixtures at atmospheric pressure. Validation against experimental data confirms the accuracy of the model, especially for discharge current characteristics, with a peak current of 2.5 mA. Time-resolved analysis revealed that CO and O<sub>2</sub> represent the major species formed during CO<sub>2</sub> splitting, while O, O<sub>3</sub>, and minor carbon-based species appear at lower concentrations. Charged species such as CO<sub>2</sub><sup>+</sup> and CO<sub>3</sub><sup>-</sup> were found to play a critical role in plasma kinetics, strongly correlating with current pulses during breakdown events. Parametric studies highlighted the influence of argon fraction, frequency, voltage, and pressure on discharge performance. Optimal CO production was obtained in CO<sub>2</sub>/Ar mixtures with 75–90% Ar, at intermediate frequencies 3 kHz, moderate pressures 760 Torr, and applied voltages up to 9 kV. These findings provide valuable insights into plasma-assisted CO<sub>2</sub> conversion, emphasizing the importance of discharge conditions in enhancing efficiency and guiding the design of DBD reactors for sustainable carbon utilization.

Copyright © 2026 by Authors, Published by BCREC Publishing Group. This is an open access article under the CC BY-SA License (<https://creativecommons.org/licenses/by-sa/4.0>).

**Keywords:** Dielectric barrier discharge; One-dimensional fluid model; Discharge current dynamics; CO<sub>2</sub> conversion

**How to Cite:** Chenoui, M., Tebani, H., Benyoucef, D. (2026). Modeling and Electrical Characterization of CO<sub>2</sub>/Ar Dielectric Barrier Discharges at Atmospheric Pressure. *Bulletin of Chemical Reaction Engineering & Catalysis*, 21 (1), 38-50. (doi: 10.9767/bcrec.20493)

**Permalink/DOI:** <https://doi.org/10.9767/bcrec.20493>

## 1. Introduction

The significant rise in the concentration of carbon dioxide (CO<sub>2</sub>) in the atmosphere, driven primarily by fossil fuel combustion and industrial activity, is a primary cause of climate change and global warming [1–3]. The mitigation of CO<sub>2</sub> emissions and its conversion into value-added products has, therefore, become a critical research priority. Conventional thermochemical and catalytic approaches often require high temperatures, pressures, or costly materials,

which limit their scalability and economic viability [4]. In this context, plasma-based technologies have emerged as attractive alternatives, offering the unique advantage of operating under mild conditions while efficiently producing reactive species that activate CO<sub>2</sub> molecules [5–7].

Among plasma methods, dielectric barrier discharges (DBDs) have attracted particular attention due to their simple configuration, scalability to large surface areas, and ability to generate non-equilibrium plasmas at atmospheric pressure [8–10]. In a DBD, the application of an alternating or pulsed high voltage across dielectric-covered electrodes produces numerous

\* Corresponding Author.

Email: [m.chenoui@univ-chlef.dz](mailto:m.chenoui@univ-chlef.dz) (M. Chenoui)

transient microdischarges. These discharges accelerate electrons to energies sufficient to excite, ionize, and dissociate CO<sub>2</sub> molecules, driving both vibrational and electronic excitation pathways [11,12]. However, the efficiency of pure CO<sub>2</sub> splitting remains low because of its high vibrational energy thresholds and rapid deactivation through vibrational–translational (V–T) relaxation processes [13].

To overcome these limitations, researchers have explored the addition of inert gases, particularly noble gases such as argon (Ar), into CO<sub>2</sub> discharges [14–16]. Ar admixture modifies the discharge dynamics by lowering the breakdown voltage, increasing plasma stability, and enhancing electron density through Penning ionization and energy-transfer collisions [17,18]. These effects broaden the electron energy distribution function (EEDF), increasing the probability of inelastic electron – CO<sub>2</sub> collisions that lead to vibrational excitation and eventual dissociation [19]. Experimental and modeling studies have demonstrated that Ar can improve CO<sub>2</sub> conversion and energy efficiency under optimized conditions, although the precise mechanisms remain the subject of ongoing investigation [20–22].

Recent numerical modeling efforts have provided valuable insights into the spatiotemporal evolution of species in DBD plasmas [23–25]. Time-dependent one-dimensional (1D) fluid models, in particular, allow detailed tracking of electron density, ion kinetics, and neutral product formation under varying

discharge conditions. These models complement experimental diagnostics by revealing microscopic discharge features that are otherwise difficult to capture, such as microdischarge lifetimes, electron heating mechanisms, and local field variations [26].

This study utilizes a time-resolved one-dimensional fluid approach model to examine the influence of argon addition on the plasma characteristics of carbon dioxide discharges at atmospheric pressure. The model provides a systematic investigation of the temporal evolution of electron density, discharge current, and species concentrations in relation to temporal evolution and discharge spacing. Special attention is given to the impact of Ar on CO production, as this represents the main target product of plasma-assisted CO<sub>2</sub> splitting. The results are discussed in the context of existing experimental studies, providing deeper insight into how the operating parameters and gas composition can be tuned to improve efficiency. Ultimately, the objective of this work is to advance the fundamental understanding of CO<sub>2</sub> plasma chemistry and to support the development of optimized plasma-based CO<sub>2</sub> conversion technologies.

## 2. Materials and Methods

### 2.1 Plasma Modeling Approach

The geometry was developed using a one-dimensional approach following the framework described in literature [27], as shown in Figure 1. The applied one-dimensional representation is further illustrated.

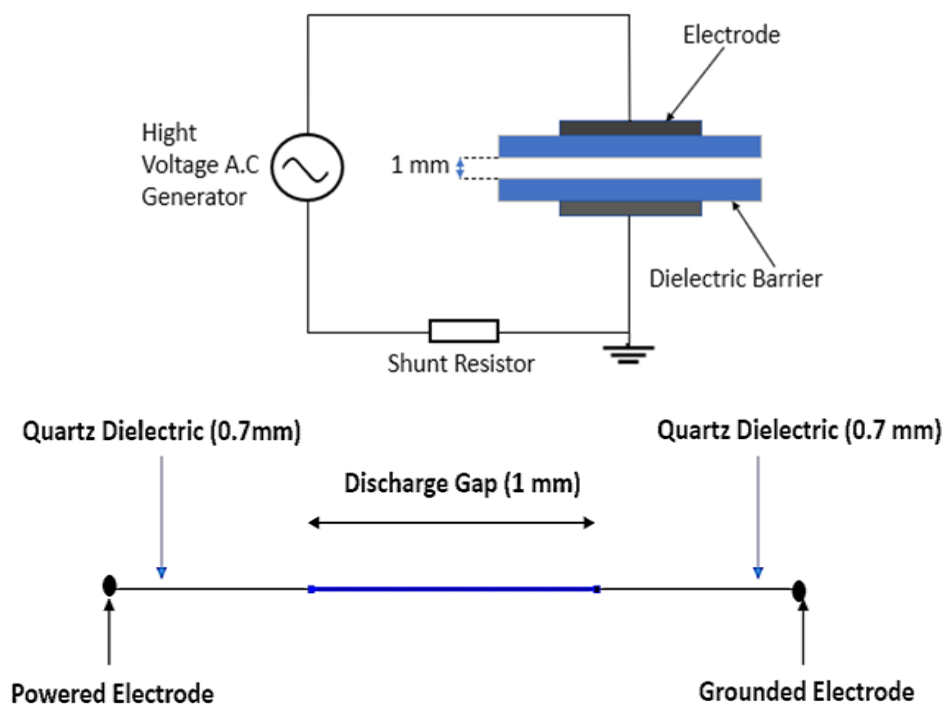


Figure 1. Schematic of the DBD setup and one-dimensional geometry applied in the simulation.

## 2.2 Model Equations

The dielectric barrier discharge model is governed by a set of coupled equations that describe the behavior of electrons, non-electron species, and the electrostatic field. Electrons, ground state atoms, ions, and excited atoms are the particles that are considered in this simulation [28-29]. The numerical simulation is founded on a one-dimensional fluid model, constructed by solving the first two moments of the Boltzmann equation in combination with Poisson's equation [30-31]. The behavior of discharge plasma is determined by:

### 2.2.1 Electron transport equations

A pair of drift-diffusion equations is solved to determine the electron density  $n_e$  and mean electron energy  $n_\epsilon$ , assuming that convection effects from fluid motion are negligible:

$$\frac{dn_e}{dt} + \nabla \cdot [-n_e \mu_e E - D_e \nabla n_e] = R_e \quad (1)$$

$$\frac{dn_\epsilon}{dt} + \nabla \cdot [-n_\epsilon \mu_\epsilon E - D_\epsilon \nabla n_\epsilon] + E \cdot \Gamma_e = R_\epsilon \quad (2)$$

Where ( $R_e$ ) is the electron source and ( $R_\epsilon$ ) is the energy loss due to inelastic collisions. The electron diffusivity ( $D_e$ ), energy mobility ( $\mu_\epsilon$ ), and energy diffusivity ( $D_\epsilon$ ) are computed from the electron mobility ( $\mu_e$ ) using the following relations:

$$D_e = \mu_e T_e, \mu_\epsilon = \left(\frac{5}{3}\right) \mu_e, D_\epsilon = \mu_\epsilon T_e \quad (3)$$

### 2.2.2 Source coefficients

The source coefficients are determined by the plasma chemistry using rate coefficients. The electron source term ( $R_e$ ) is determined by:

$$R_e = \sum_{i=1}^M x_i k_i N_n n_e \Delta \epsilon_i \quad (4)$$

With ( $\Delta \epsilon_i$ ) indicates the energy loss from reaction (i) The rate coefficients are evaluated from cross-section data available on the LXCAT database using the following integral expression.

$$k_k = \gamma \int_0^\infty \epsilon \sigma_k(\epsilon) f(\epsilon) d\epsilon \quad (5)$$

Where ( $f$ ) the electron energy distribution function (EEDF) and ( $\sigma$ ) collision cross section ( $m^2$ ) with:

$$\gamma = \sqrt{\frac{2q}{m_e}} \quad (6)$$

With  $q$  represents the electron charge (c), and ( $m_e$ ) corresponds to the electron mass (kg).

### 2.2.3 Electrostatic field

$$-\nabla \cdot \epsilon_0 \epsilon_r \nabla v = \rho \quad (7)$$

$\rho$  represents the charge density, which is the amount of electric charge per unit volume in a given space,  $\epsilon_0$  represent permittivity of free space, and  $\epsilon_r$  permittivity of material dielectric:

$$\rho = q(\sum_{k=1}^N Z_k n_k - n_e) \quad (8)$$

with  $Z_k$  is the electric charge,  $q$  is the absolute value of electronic charge.

### 2.2.4 Non-electron species transport

The evolution of the mass fraction for all non-electron species is obtained by solving the following equation.

$$\rho \frac{\partial w_k}{\partial t} + \nabla \cdot (\rho \mu w_k) + \nabla \cdot j_k = R_k \quad (9)$$

where  $w_k$  is the mass fraction for species  $k$ ,  $j_k$  is the diffusive flux vector for species  $k$ , and  $R_k$  is the rate expression for species  $k$ .

### 2.2.5 Boundary conditions

The electron flux to the electrodes and all reactor walls:

$$-n \cdot \Gamma_e = \frac{1}{2} V_{e,th} n_e - \sum_p \gamma_p (\Gamma_p \cdot n) \quad (10)$$

$\gamma_p$  denotes the secondary electron emission coefficient, while  $n$  represents the unit normal vector to the wall. The electron thermal velocity,  $V_{e,th}$ , is expressed as:

$$V_{e,th} = \sqrt{\frac{K_B T_e}{\pi m_e}} \quad (11)$$

### 2.2.6 Electric potential

The driven electrode receives an electric potential:

$$V = V_0 \sin(2 \cdot \pi \cdot f \cdot t) \quad (12)$$

### 2.2.7 Ion mobilities

The standard formula for calculating ion mobility using polarizability is based on the Langevin polarization capture theory [32]:

$$K = 13.88 \times \sqrt{\frac{1}{\alpha \times \mu}} \quad (13)$$

where  $K$  ion mobility ( $cm^2/V.s$ ) and  $\alpha$  polarizability of neutral gas ( $\text{\AA}^3$ ),  $\mu$  reduced mass of the ion-neutral pair ( $u$ ).

$$\mu = \frac{M_{ion} \times M_{neutral}}{M_{ion} + M_{neutral}} \quad (14)$$

$$\frac{1}{\mu_{mix}} = \frac{\eta_1}{\mu_1} + \frac{\eta_2}{\mu_2} \quad (15)$$

$\eta_1$  and  $\eta_2$  represent the molar fractions of gases 1 and 2, while  $\mu_1$  and  $\mu_2$  denote their respective ion mobilities.

### 2.3 Plasma Chemistry

The plasma chemistry implemented in the model comprising a detailed set of 108 reactions involving 19 species presented in Table 1 accounts for the key electron–molecule, ion–molecule, and neutral–neutral processes governing CO<sub>2</sub> conversion in dielectric barrier discharges. In particular, electron impact reactions such as ionization, excitation, and dissociation of CO<sub>2</sub> and Ar are included presented in Table 2, as they provide the primary pathway for generating reactive species.

Table 1. Species in CO<sub>2</sub>/Ar model.

Neutral	Negative ions	Positive ions	Exited space
C, O, CO <sub>2</sub> , O <sub>2</sub> , O <sub>3</sub> , CO, C <sub>2</sub> O	e <sup>-</sup> , O <sup>-</sup> , O <sub>2</sub> <sup>-</sup> , O <sub>3</sub> <sup>-</sup> , CO <sub>3</sub> <sup>-</sup> , CO <sub>4</sub> <sup>-</sup>	CO <sub>2</sub> <sup>+</sup> , O <sup>+</sup> , O <sub>2</sub> <sup>+</sup> , Ar <sup>+</sup> , Ar <sub>2</sub> <sup>+</sup>	Ars

Table 2. Reactions explored in the model and their rate coefficients in (m<sup>6</sup>/s) and (m<sup>3</sup>/s) for three-body and two-body respectively, CO<sub>2</sub> (X,v=1-16) refers to the first 16 vibrationally excited states of CO<sub>2</sub>.

No	Reaction	Reaction rate	References
Elastic and ionization electron-impact reactions			
X1	e <sup>-</sup> + CO <sub>2</sub> → CO + O <sup>-</sup>	Cross section	[33]
X2	e <sup>-</sup> + CO <sub>2</sub> → e <sup>-</sup> + CO <sub>2</sub> (X,v=1-16)	Cross section	[33]
X3	e <sup>-</sup> + CO <sub>2</sub> → 2e <sup>-</sup> + CO <sub>2</sub> <sup>+</sup>	Cross section	[33]
X4	e <sup>-</sup> + CO <sub>2</sub> → e <sup>-</sup> + CO + O	Cross section	[33]
X5	e <sup>-</sup> + CO → e <sup>-</sup> + CO	Cross section	[33]
X6	e <sup>-</sup> + O <sub>3</sub> → e <sup>-</sup> + O <sub>3</sub>	Cross section	[33]
X7	e <sup>-</sup> + O <sub>2</sub> → e <sup>-</sup> + O <sub>2</sub>	Cross section	[33]
X8	e <sup>-</sup> + O → e <sup>-</sup> + O	Cross section	[33]
X9	e <sup>-</sup> + Ar → Ar + e <sup>-</sup>	Cross section	[33]
X10	e <sup>-</sup> + Ar → Ars + e <sup>-</sup>	Cross section	[33]
X11	e <sup>-</sup> + Ar → Ar <sup>+</sup> + 2e <sup>-</sup>	Cross section	[33]
X12	e <sup>-</sup> + Ars → Ar <sup>+</sup> + 2e <sup>-</sup>	Cross section	[33]
X13	e <sup>-</sup> + Ars → Ar + e <sup>-</sup>	Cross section	[33]
Electron–atom or molecule interactions			
E1	e <sup>-</sup> + Ar + Ar <sup>+</sup> → Ar + Ar	1.0×10 <sup>-36</sup>	[34,36]
E2	e <sup>-</sup> + CO <sub>2</sub> <sup>+</sup> → CO + O	2.0×10 <sup>-11</sup> /(√T <sub>e</sub> ×T <sub>g</sub> )	[34,35]
E3	e <sup>-</sup> + CO <sub>2</sub> <sup>+</sup> → C + O <sub>2</sub>	3.94×10 <sup>-13</sup> ×T <sub>e</sub> <sup>-0.4</sup>	[35]
E4	e <sup>-</sup> + O <sub>2</sub> → 2e <sup>-</sup> + O <sub>2</sub> <sup>+</sup>	1.8×10 <sup>-17</sup>	[36]
Ion-ion and ion-neutral reactions			
I1	Ars + Ar → Ar + Ar	3.0×10 <sup>-21</sup>	[35]
I2	Ars + Ars → e <sup>-</sup> + Ar <sup>+</sup> + Ar	1.625×10 <sup>-16</sup> /√T <sub>g</sub>	[35]
I3	2Ar + Ar <sup>+</sup> → Ar <sub>2</sub> <sup>+</sup> + Ar	2.5×10 <sup>-43</sup>	[36]
I4	Ar <sub>2</sub> <sup>+</sup> + Ar → Ar <sup>+</sup> + 2Ar	2.496×10 <sup>-36</sup>	[36]
I5	Ar <sup>+</sup> + CO <sub>2</sub> → Ar + CO <sub>2</sub> <sup>+</sup>	7.6×10 <sup>-16</sup>	[35]
I6	Ar + CO <sub>2</sub> → CO + O + Ar	1.27×10 <sup>-44</sup> / (T <sub>g</sub> /300) × exp(-170/ T <sub>g</sub> )	[36,35]
I7	O <sub>2</sub> <sup>+</sup> + Ar → e <sup>-</sup> + O <sub>2</sub> <sup>+</sup> + Ar	2.7×10 <sup>-16</sup> √(T <sub>g</sub> /300) × exp(-5590/ T <sub>g</sub> )	[35]
I8	O <sub>2</sub> <sup>+</sup> + O <sub>2</sub> <sup>+</sup> → O + O + O <sub>2</sub>	4.2×10 <sup>-13</sup>	[36,34]
I9	O <sub>2</sub> <sup>+</sup> + CO <sub>2</sub> <sup>+</sup> → CO + O <sub>2</sub> + O	6.0×10 <sup>-13</sup>	[36]

### 2.4 Plasma Electrical Properties

Analysis of Dielectric Barrier Discharge Behavior in pure CO<sub>2</sub> under atmospheric conditions was carried out using the same experimental configuration as in literature [27], allowing comparison and validation of the present simulation model, examined a 1D geometry made up of two parallel plates and under a wide spectrum of discharge parameters and operating environments relevant to atmospheric pressure plasmas presented in Table 3.

### 3. Results and Discussion

The spatiotemporal characteristics of DBD in pure CO<sub>2</sub> have been numerically studied. The simulation is carried for atmospheric pressure, external voltage amplitude of 6 kV, frequency of 2 kHz and a gas temperature equal to 300 K.

I10	$O^- + CO \rightarrow CO_2 + e$	$5.5 \times 10^{-16}$	[35]
I11	$O^- + O_2 \rightarrow O_3 + e$	$1.0 \times 10^{-18}$	[35]
I12	$O^- + O_3 \rightarrow O_2 + O_2 + e$	$3.0 \times 10^{-16}$	[35]
I13	$O^- + CO_2 + CO_2 \rightarrow CO_3^- + CO_2$	$9.0 \times 10^{-35}$	[36,35]
I14	$Ar^{++} + CO \rightarrow CO^+ + Ar$	$9.0 \times 10^{-17}$	[37]
I15	$Ar^{++} + O \rightarrow O^+ + Ar$	$0.64 \times 10^{-17}$	[37]
I16	$Ar^{++} + O_2 \rightarrow O_2^+ + Ar$	$4.6 \times 10^{-17}$	[37]
I17	$Ar_2^{++} + CO_2 \rightarrow CO_2^+ + 2Ar$	$1.1 \times 10^{-15}$	[37]
I18	$Ar_2^{++} + CO \rightarrow CO^+ + 2Ar$	$8.5 \times 10^{-16}$	[37]
I19	$Ar_2^{++} + O_2 \rightarrow O_2^+ + 2Ar$	$1.2 \times 10^{-16}$	[37]
I20	$O_2^- + O_2^+ \rightarrow O_2 + O_2$	$2.0 \times 10^{-13}$	[36,34]
I21	$O_2^- + O_3 \rightarrow O_2 + O_3^-$	$4.0 \times 10^{-16}$	[36,34]
I22	$O^+ + CO_2 \rightarrow O_2^+ + CO$	$9.4 \times 10^{-16}$	[36,34]
I23	$O^+ + CO_2 \rightarrow CO_2^+ + O$	$4.5 \times 10^{-16}$	[36,34]
I24	$CO_2^+ + O \rightarrow O^+ + CO_2$	$9.62 \times 10^{-17}$	[36,34]
I25	$CO_2^+ + O_2 \rightarrow O_2^+ + CO_2$	$5.3 \times 10^{-17}$	[36,34]
I26	$O_3^- + O \rightarrow O_2 + O_2^-$	$1.0 \times 10^{-16}$	[36,34]
I27	$O_2^+ + CO_3^- \rightarrow CO_2 + O_2 + O$	$3.0 \times 10^{-13}$	[36,34]
I28	$CO_3^- + O \rightarrow CO_2 + O_2^-$	$8.0 \times 10^{-17}$	[36,34]
I29	$CO_3^- + CO_2^+ \rightarrow CO_2 + CO_2 + O$	$5.0 \times 10^{-13}$	[36,34]
I30	$CO_4^- + O \rightarrow CO_3^- + O_2$	$1.1 \times 10^{-16}$	[36,34]
I31	$O^- + O_2^+ \rightarrow O + O + O$	$2.6 \times 10^{-14}$	[36,34]
I32	$CO_4^- + O \rightarrow CO_2 + O_2 + O^-$	$1.4 \times 10^{-17}$	[36,34]
I33	$CO_4^- + CO_2^+ \rightarrow 2CO_2 + O_2$	$5.0 \times 10^{-13}$	[36,34]
I34	$O_2^+ + CO_4^- \rightarrow CO_2 + O_2 + O_2$	$3.0 \times 10^{-13}$	[36,34]
I35	$O^- + O_3 \rightarrow O + O_3^-$	$5.3 \times 10^{-16}$	[36,34]
I36	$O_2^- + CO_2 + CO_2 \rightarrow CO_4^- + CO_2$	$1.0 \times 10^{-35}$	[36,34]
I37	$O_2^- + O^+ + CO_2 \rightarrow O_3 + CO_2$	$2.0 \times 10^{-37}$	[36,34]
I38	$O^- + O^+ \rightarrow O + O$	$4.0 \times 10^{-14}$	[36,34]
I39	$O^+ + CO_2 \rightarrow O_2^+ + CO$	$9.4 \times 10^{-16}$	[36,34]
I40	$O^+ + CO_2 \rightarrow CO_2^+ + O$	$4.5 \times 10^{-16}$	[36,34]
I50	$CO_4^- + O_3 \rightarrow CO_2 + O_3^- + O_2$	$1.0 \times 10^{-16}$	[36,34]
I51	$O_2^- + CO_2 \rightarrow O_2 + CO_2 + e$	$2.7 \times 10^{-16} \sqrt{(T_g/300)} \times \exp(-5590/T_g)$	[35]
I52	$CO_4^- + O \rightarrow CO_2 + O_3^-$	$1.4 \times 10^{-16}$	[36,34]
I53	$O_3^- + O \rightarrow O_3 + O^-$	$1.0 \times 10^{-19}$	[36,34]
Neutral-neutral reactions			
N1	$CO_2 + CO_2 \rightarrow CO + O + CO_2$	$3.91 \times 10^{-16} \exp(-49430/T_g)$	[38]
N2	$CO_2 + O_2 \rightarrow CO + O + O_2$	$1.81 \times 10^{-16} \exp(-49000/T_g)$	[38]
N3	$CO_2 + C \rightarrow CO + CO$	$1.0 \times 10^{-21}$	[35]
N4	$CO_2 + O \rightarrow CO + O_2$	$2.8 \times 10^{-17} \exp(-26500/T_g)$	[38]
N5	$CO + O + CO_2 \rightarrow CO_2 + CO_2$	$16.4 \times 10^{-46} \exp(-1510/T_g)$	[38]
N6	$CO + O + CO \rightarrow CO_2 + CO$	$8.2 \times 10^{-46} \exp(-1510/T_g)$	[38]
N7	$CO + O + O_2 \rightarrow CO_2 + O_2$	$8.2 \times 10^{-46} \exp(-1510/T_g)$	[38]
N8	$CO + O_2 \rightarrow CO_2 + O$	$4.2 \times 10^{-18} \exp(-24000/T_g)$	[38]
N9	$O + O_2 + O_2 \rightarrow O_3 + O_2$	$5.85 \times 10^{-46}$	[36]
N10	$O + O_2 + CO_2 \rightarrow O_3 + CO_2$	$1.81 \times 10^{-45}$	[36]
N11	$O + O + CO_2 \rightarrow O_2 + CO_2$	$1.04 \times 10^{-44}$	[36]
N12	$CO + Ar \rightarrow C + O + Ar$	$1.52 \times 10^{-10} (T_g/298)^{-3.1} \exp(-129000/T_g)$	[36]
N13	$CO_2 + Ar \rightarrow CO + O + Ar$	$1.27 \times 10^{-44} (T_g/300)^{-1} \exp(-170/T_g)$	[36]
N14	$O + O + Ar \rightarrow O_2 + Ar$	$4.39 \times 10^{-13} \exp(65000/T_g)$	[36]
N15	$O_2 + O + Ar \rightarrow O_3 + Ar$	$3.6 \times 10^{-46} (T_g/300)^{-1.93}$	[35]
N16	$O_2 + C_2O \rightarrow CO_2 + CO$	$3.3 \times 10^{-19}$	[34]
N17	$O + C + Ar \rightarrow CO + Ar$	$2.14 \times 10^{-41} (T_g/300)^{-3.08} \exp(-2114/T_g)$	[35]
N18	$CO_2 + CO \rightarrow CO + O + CO$	$1.81 \times 10^{-16} \exp(-49000/T_g)$	[38]
N19	$O_3 + O \rightarrow O_2 + O_2$	$8.5 \times 10^{-21}$	[35]
N20	$CO + O_3 \rightarrow CO_2 + O_2$	$4.0 \times 10^{-31}$	[35]
N21	$O + O_3 \rightarrow O_2 + O_2$	$8.5 \times 10^{-21}$	[35]
N22	$CO_2 + C + CO \rightarrow C_2O + CO_2$	$6.3 \times 10^{-44}$	[36]
N23	$O + C_2O \rightarrow CO + CO$	$5 \times 10^{-17}$	[36]

Figure 2 shows the total current of the dielectric barrier discharge in pure carbon dioxide reveals a clear correlation between the applied voltage, gas voltage, and the discharge current. As illustrated, the applied sinusoidal voltage drives the plasma dynamics, while the gas voltage shows a distinct phase shift due to the dielectric barrier effect, highlighting the capacitive nature of the discharge, the simulated current in the second AC cycle. Breakdown occurs on the rising negative flank, with a sharp current pulse peaking at 0.55 ms, the simulated peak current is 2.5 mA and display good agreement with measured current.

Figure. 3 show Time evolution of the power density the maximum power deposition reaches approximately 4 W/cm<sup>3</sup>, after which it decreases rapidly to near zero before the next cycle begins. This behavior is characteristic of capacitive (non-thermal) discharges [39], where energy is stored in the dielectric and suddenly released into the plasma during breakdown, the asymmetry in peak intensity with the first peak being slightly higher than subsequent ones-suggests stronger initial charging of the dielectric surface. over time, surface charge accumulation modifies the local electric field, leading to slightly reduced subsequent breakdown intensity but maintaining periodicity.

### 3.1 Temporal variation of plasma species densities

To assess the effect of argon dilution on the discharge dynamics, a comparative analysis was carried out in (90% CO<sub>2</sub> 10% Ar) gas mixture under identical operating conditions of pure CO<sub>2</sub>. Figure 4a presents the time-dependent behavior of neutrals species number densities in 100 period. The results indicate rapid formation of CO and O<sub>2</sub>, which reach steady-state concentrations on the order of 10<sup>20</sup> m<sup>-3</sup>, confirming their roles as primary products of CO<sub>2</sub> dissociation. Atomic

oxygen O and ozone O<sub>3</sub> exhibit intermediate concentrations, with O<sub>3</sub> showing a gradual increase and a transient fluctuation around 0.03 s, likely due to recombination dynamics. Trace species such as atomic carbon C and carbon suboxide C<sub>2</sub>O remain at much lower levels

Figure 4b displays the transient evolution of selected charged species and current over one full AC cycle during CO<sub>2</sub> dielectric barrier discharge operation. The numerical analysis highlights that the densities of the negative ions CO<sub>3</sub><sup>-</sup> and CO<sub>4</sub><sup>-</sup> increase sharply during the discharge pulses, reaching peak values around 10<sup>20</sup> m<sup>-3</sup>. Electron density follows a similar temporal profile, albeit at slightly lower magnitudes 10<sup>15</sup> m<sup>-3</sup>, reflecting the influence of ionization and attachment processes during breakdown events. The density of O<sub>2</sub><sup>-</sup> remains relatively low and stable, suggesting limited contribution from oxygen-based negative ion chemistry under the considered conditions. The current profile black curve, right axis exhibits two sharp peaks per cycle, corresponding to the breakdown phases during the positive and negative phases of the applied voltage cycle, consistent with typical DBD behavior. The temporal correlation between the current peaks and the rise in charged species highlights the strong coupling between plasma kinetics and electrical response in the reactor

Figure. 4c depicts the densities of CO<sub>2</sub> derived positive ions. CO<sub>2</sub><sup>+</sup> is the most abundant ion peaking at 10<sup>16</sup>-10<sup>17</sup> m<sup>-3</sup>, formed mainly by electron impact ionization and Penning reactions, followed by O<sub>2</sub><sup>+</sup> 10<sup>13</sup> m<sup>-3</sup> produced via dissociation and recombination pathways, whereas CO<sup>+</sup> remains a minor species. Figure 4d shows the evolution of argon species a high density of Ar metastable 10<sup>15</sup> m<sup>-3</sup> forms rapidly at each ignition peak and decays slowly between discharges, playing a key role in sustaining the plasma

Table 3. Discharge parameters considered in this study.

Parameters	Value
Maximum applied voltage	6,8,9 (kV)
Frequency	2,3,4 (kHz)
Resistance	1 (kΩ)
Pressure	500,760,1000 (Torr)
Discharge gap	1 (mm)
Electrode area	9 (cm <sup>3</sup> )
Preionization density	10 <sup>6</sup> (m <sup>3</sup> )
Thickness of dielectric	0.7 (mm)
Relative permittivity of dielectric	4.2
Molar mass CO <sub>2</sub> ,Ar respectively	0.04401 , 0.04 (kg/mol)
Polarizability CO <sub>2</sub> ,Ar respectively	2.91 ,1.64 (Å <sup>3</sup> )
Gas temperature	300 (K)
Gas mixture content CO <sub>2</sub> /Ar with Ar percentage	90 , 75 ,50 ,25 ,10 (%)

through Penning ionization of CO<sub>2</sub>. Ar<sup>+</sup> ions are only transient and are immediately converted into Ar<sub>2</sub><sup>+</sup> dimer ions, which become the predominant argon positive ion with densities reaching 10<sup>12</sup> m<sup>-3</sup>.

### 3.2 Analysis of Operating Parameters

A comprehensive parametric study was performed to analyze the impact of key operating conditions on the behavior of the dielectric barrier discharge in a CO<sub>2</sub>/Ar mixture at atmospheric pressure. Operating conditions including applied voltage, excitation frequency, gas pressure, and gas composition were systematically varied in order to assess their impact on electrical characteristics and species densities.

#### 3.2.1 Influence of Ar dilution

In this analysis, the operating conditions were fixed at 6 kV applied voltage, 2 kHz frequency, and 760 Torr pressure, while the argon concentration was systematically adjusted between 10% and 90%, the effect of argon admixture on CO<sub>2</sub> dielectric barrier discharge performance is shown in Figure 5a. Increasing the

Ar fraction significantly modifies the discharge behavior, the current waveforms exhibit higher amplitudes in Ar rich mixtures, attributed to the lower ionization threshold of Ar and the efficient generation of electron avalanches, this is consistent with the strong increase in electron density as shown in Figure 5b, which rises by nearly seven orders of magnitude when the Ar content increases from 10% to 90%. The higher electron population promotes more efficient electron-impact dissociation of CO<sub>2</sub>, as confirmed by the CO density profiles. Maximum CO concentrations are obtained in mixtures containing 75–90% Ar, where CO production reaches the order of 10<sup>18</sup>–10<sup>19</sup> m<sup>-3</sup> as shown in Figure 5c where the balance between electron impact excitation and vibrational energy transfer is optimized at higher Ar contents, CO<sub>2</sub> depletion limits vibrational pathways, while higher CO<sub>2</sub> fractions increase collisional quenching.

#### 3.2.2 Influence of frequency

For this analysis, the applied voltage 6 kV, Ar fraction 10%, and pressure 760 Torr were kept constant, while the frequency was varied from 2 to 4 kHz, The effect of discharge frequency on the

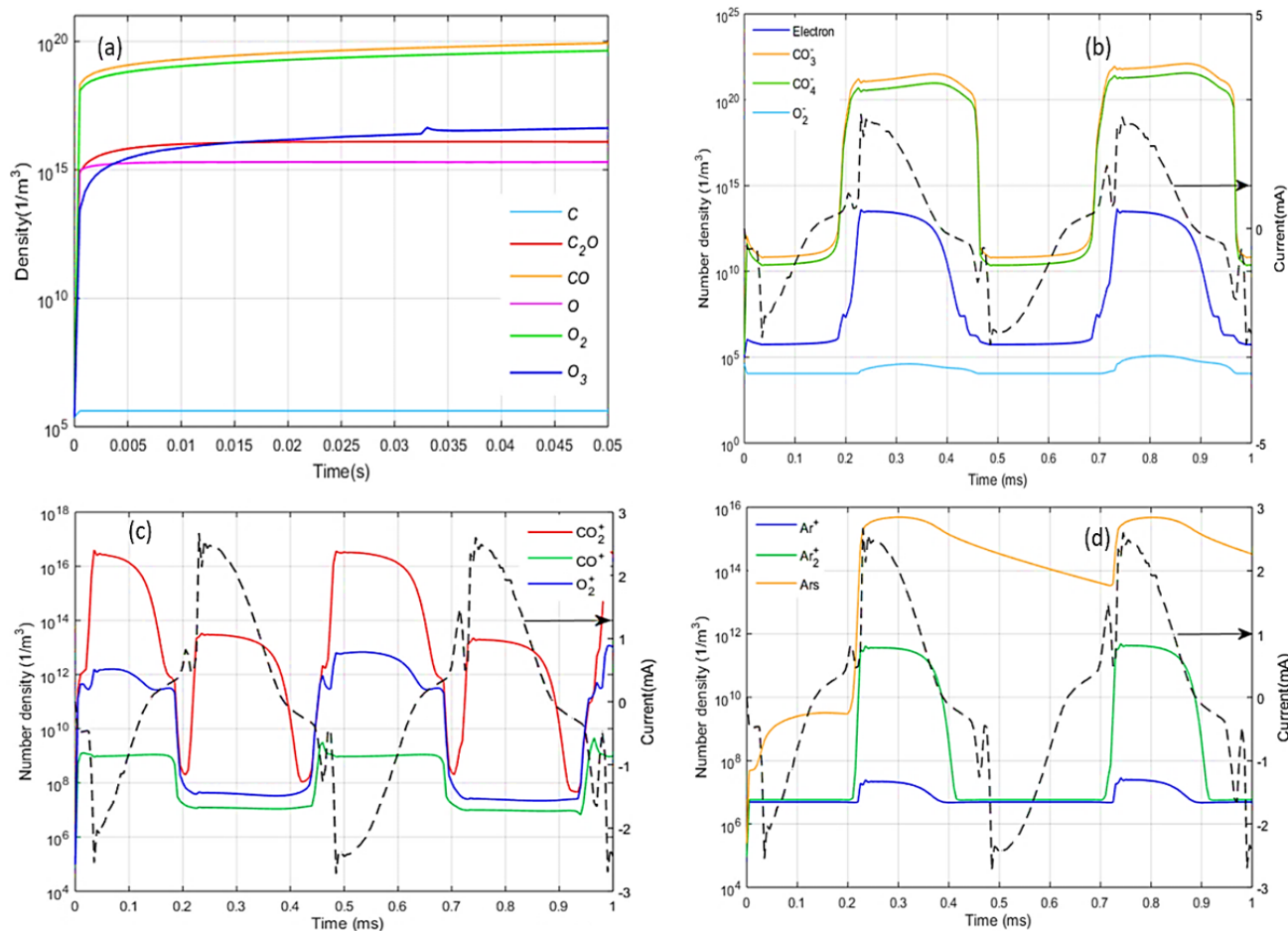


Figure 4. Time evolutions of the discharge species: (a) neutral species; (b,) CO<sub>2</sub>-derived negative ions, (c) CO<sub>2</sub>-derived positive ions and (d) Ar excited species and positive ions.

temporal evolution and spatial characteristics of the DBD plasma for CO<sub>2</sub> conversion is presented in Figure 6. At the lower frequency of 2 kHz, the current waveform exhibits a smoother and less pronounced profile, with only moderate peak amplitudes, as shown in Figure 6a. Correspondingly, Figure 6b shows that the electron density remains relatively low, on the order of 10<sup>8</sup>–10<sup>9</sup> m<sup>-3</sup>, and Figure 6c indicates that CO formation is limited under these conditions. When the frequency is increased to 3 kHz, the discharge becomes significantly more energetic, displaying higher and sharper current peaks with increasing frequency, as illustrated in Figure 6a. This enhancement is accompanied by a substantial rise in electron density up to 10<sup>12</sup> m<sup>-3</sup> near the cathode Figure 6b. This enhanced electron population promotes more effective CO<sub>2</sub> dissociation, leading to higher CO densities across the discharge gap as shown in Figure 6c. However, at higher frequency 4 kHz, although the current amplitude is further amplified with pronounced fluctuations, the electron density decreases compared to 3 kHz, indicating reduced discharge stability. Consequently, CO production is slightly more than at 3 kHz. These results suggest that an

intermediate frequency 3 kHz provides the optimal balance between discharge intensity and stability, leading to the most efficient CO<sub>2</sub> conversion in the DBD reactor.

### 3.2.3 Influence of applied voltage

For this analysis, the frequency 2 kHz, Ar fraction 10%, and pressure 760 Torr were kept constant, while the applied voltage was varied from 6 to 9 kV, Figure 7a shows the discharge current waveforms for applied voltages of 6, 8, and 9 kV. The current exhibits the typical periodic behavior of filamentary DBDs, voltage enhances the discharge current amplitude, indicating stronger microdischarge activity with increasing voltage. although a partial saturation is observed at the highest level (9 kV) because the discharge begins to exhibit reduced stability beyond this threshold. Figure 7b shows a higher applied voltages significantly enhance the electron density, increasing it by multiple orders of magnitude, which promotes more efficient CO<sub>2</sub> dissociation, CO production increases significantly with voltage, as shown in Figure 7c.

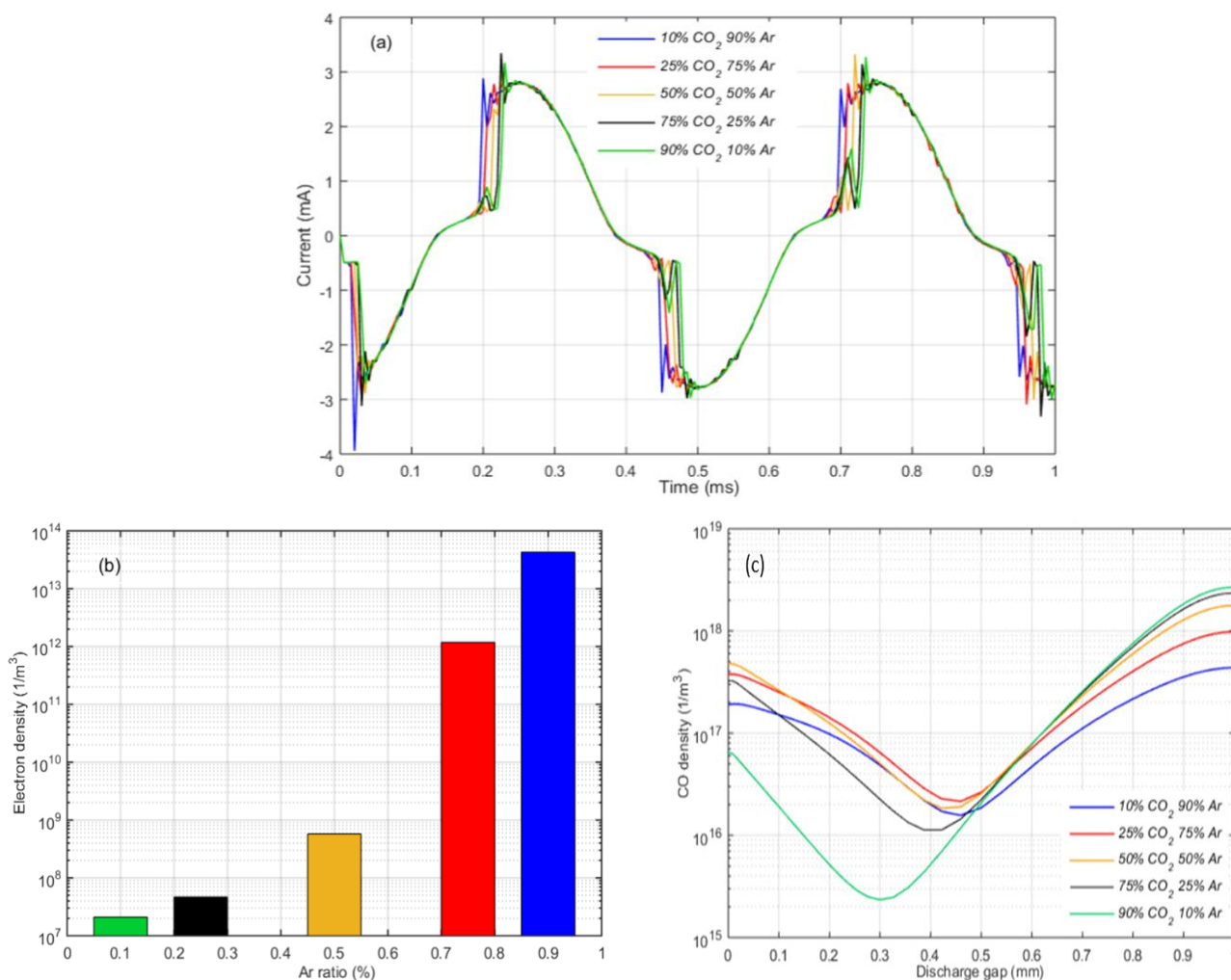


Figure 5. Effect Ar Dilution on: (a) Current waveform, (b) Electron concentration, (c) CO concentration.

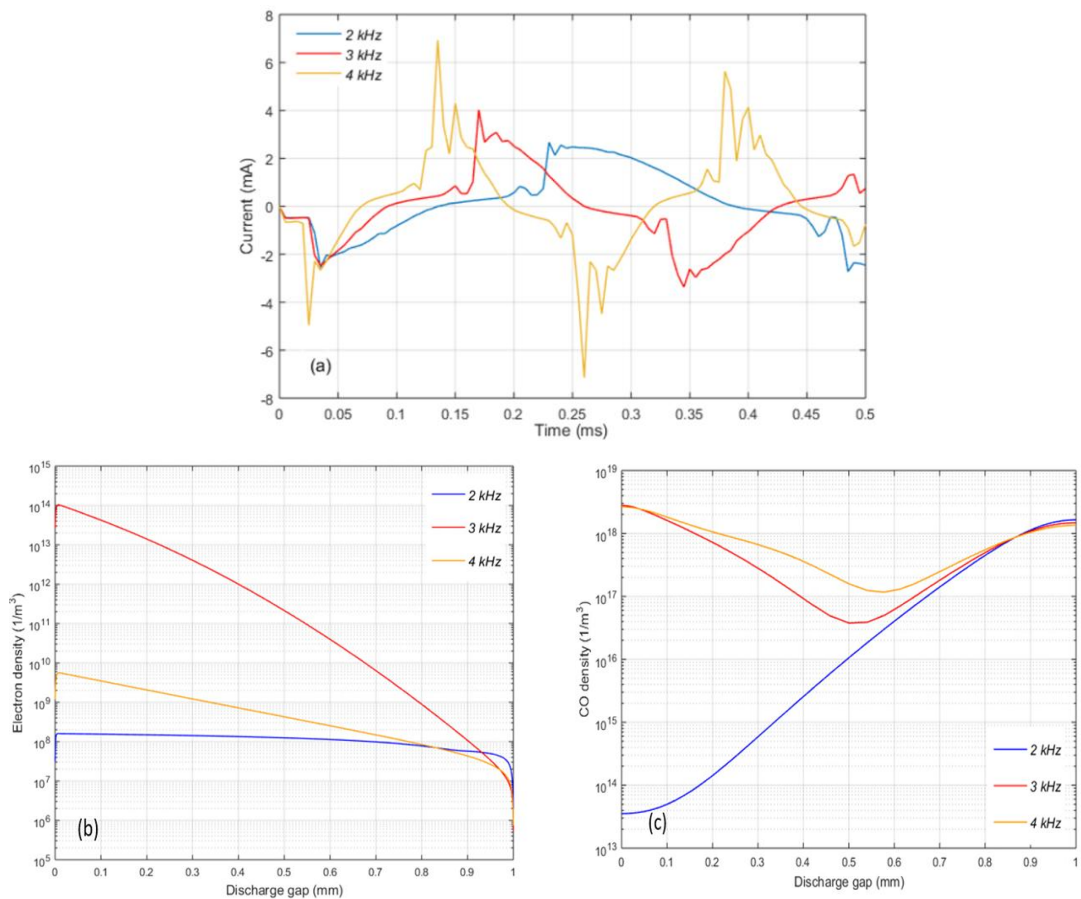


Figure 6. Effect frequency on: (a) Current waveform, (b) Electron concentration, (c) CO concentration.

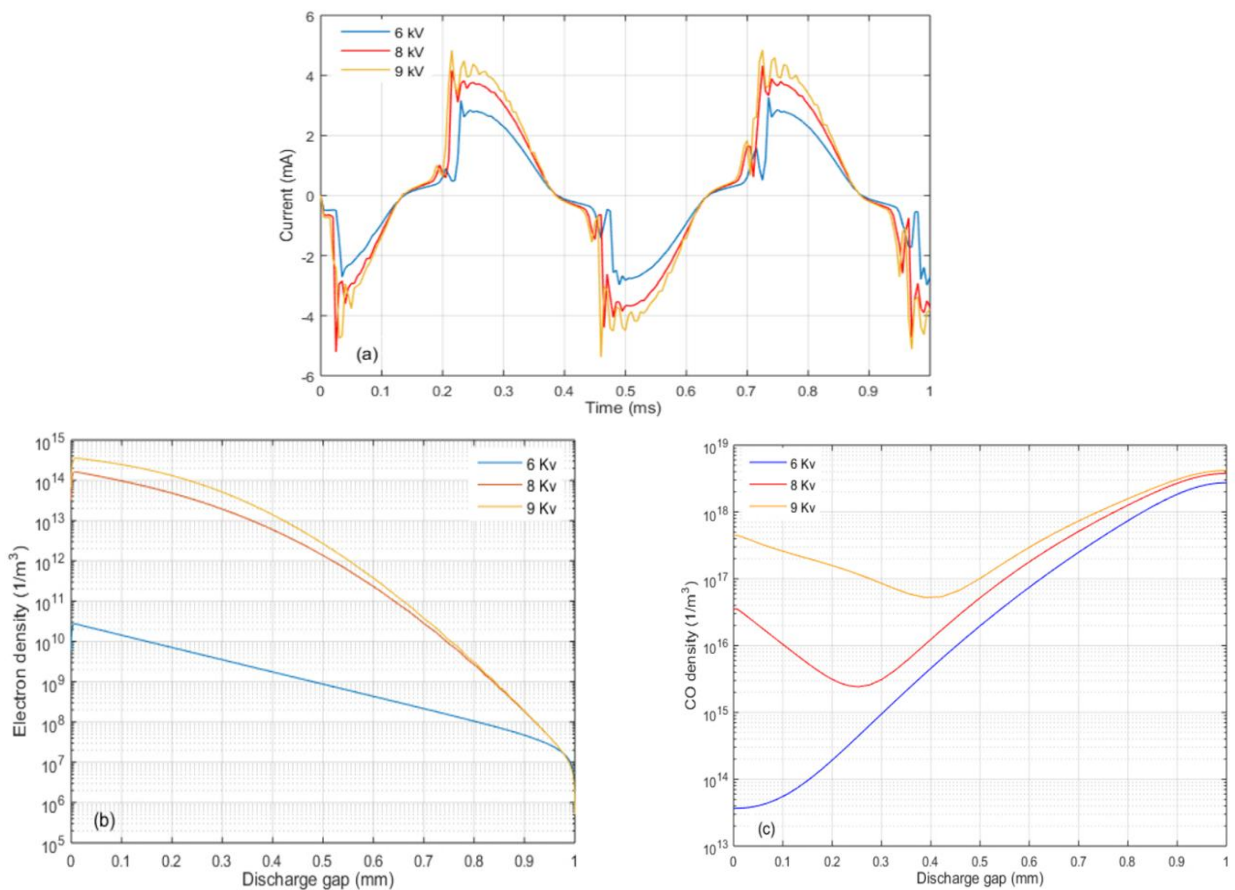


Figure 7. Effect of applied voltage on: (a) Current waveform, (b) Electron concentration, (c) CO concentration.

### 3.2.4 Influence of Gas Pressure

For this study, the applied voltage 6 kV, frequency 2 kHz, and Ar fraction 10 % were maintained constant, and only the gas pressure was varied, ranging from 500 to 1000 Torr, Figure 8a illustrates at 500 Torr, the current pulses appear sharper, reflecting higher electron mobility and reduced collisional damping. In contrast, at 1000 Torr, the waveforms broaden due to enhanced electron-neutral collisions, which slow down charge transport. The 760 Torr case, corresponding to atmospheric pressure, lies in between these two regimes.

The spatial distribution of electron density is shown in Figure 8b. At 500 Torr, the electron density reaches approximately  $10^{14} \text{ m}^{-3}$  near the cathode and decays gradually across the 1 mm discharge gap. Increasing the pressure to 760 Torr reduces the initial density to  $10^{13} \text{ m}^{-3}$ , with a steeper decay profile. At 1000 Torr, the electron density falls to  $10^{11} \text{ m}^{-3}$ , with a rapid decrease along the discharge length. These results confirm the strong influence of collisional processes at higher pressures, which shorten the electron mean free path and suppress ionization rates.

The effect of pressure on CO production is presented in Figure 8c. For 500 Torr, the CO density increases steadily with the discharge gap, achieving values above  $10^{17} \text{ m}^{-3}$ , indicating efficient  $\text{CO}_2$  splitting under low-pressure conditions. At atmospheric pressure 760 Torr, CO formation remains significant but is reduced to  $10^{16}$  at 1000 Torr, however, CO densities decrease sharply to  $10^{14} \text{ m}^{-3}$ , confirming that high collisional quenching suppresses the generation of reactive species.

achieving values above  $10^{17} \text{ m}^{-3}$ , indicating efficient  $\text{CO}_2$  splitting under low-pressure conditions. At atmospheric pressure 760 Torr, CO formation remains significant but is reduced to  $10^{16}$  at 1000 Torr, however, CO densities decrease sharply to  $10^{14} \text{ m}^{-3}$ , confirming that high collisional quenching suppresses the generation of reactive species.

## 4. Conclusion

This study investigated the electrical and physicochemical behavior of dielectric barrier discharges in pure  $\text{CO}_2$  and  $\text{CO}_2/\text{Ar}$  mixtures at atmospheric pressure through simulation and comparison with experimental data. The results confirmed that the model successfully reproduces key discharge behaviors, including the phase shift between applied and gas voltage, current peaks correlated with plasma breakdown, and the formation of major products, such as CO and  $\text{O}_2$ . Parametric analyses revealed that argon addition significantly enhances electron density and CO production, frequency strongly influences discharge stability with optimal conversion around 3 kHz, applied voltage increases dissociation efficiency up to a saturation point, where further voltage increase no longer improves  $\text{CO}_2$  conversion due to energy losses in gas heating

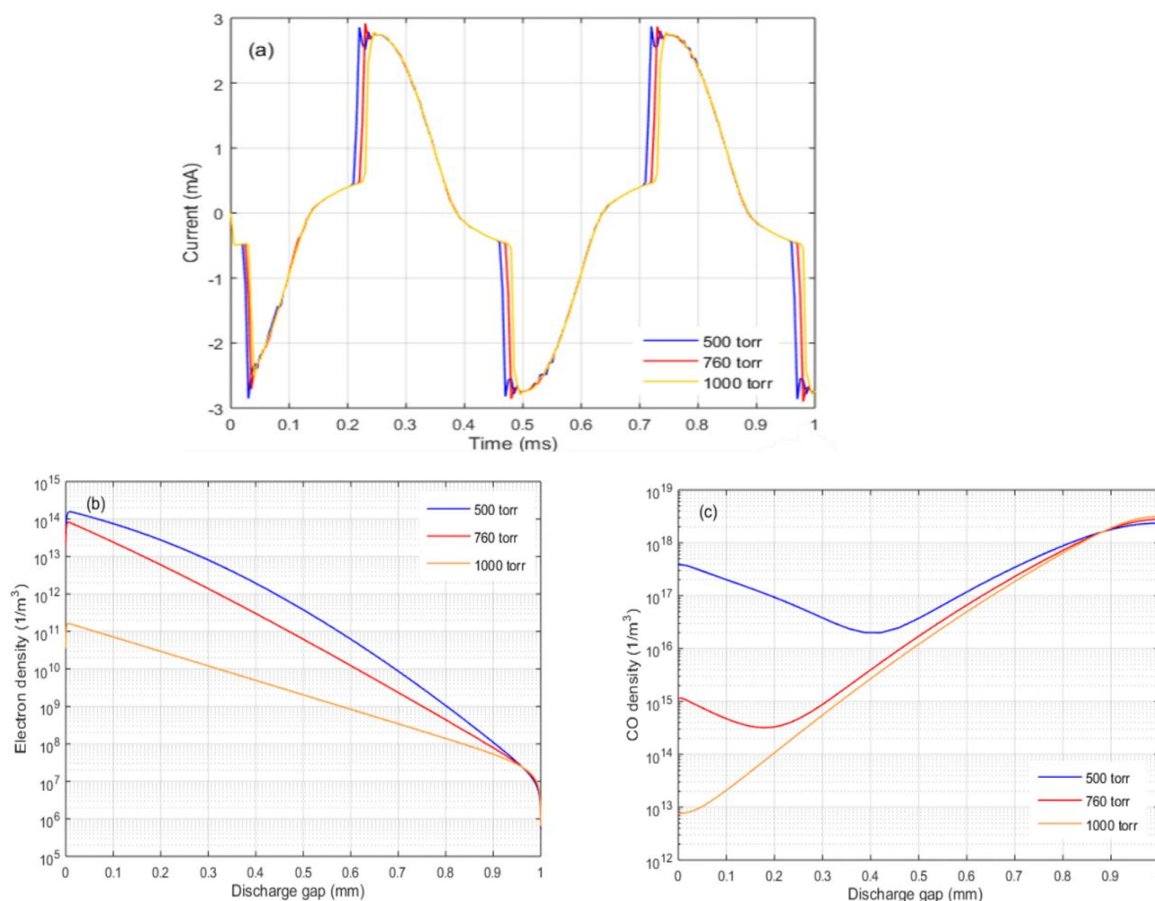


Figure 8. Effect of the gas pressure on: (a) current waveform, (b) electron concentration, (c) CO concentration.

and recombination and higher pressures suppress CO<sub>2</sub> conversion due to collisional quenching. Overall, the findings highlight the importance of optimizing operating parameters particularly Ar concentration, frequency, and applied voltage to achieve efficient CO<sub>2</sub> splitting in DBD reactors, offering valuable insights for the design of plasma-based CO<sub>2</sub> conversion systems.

### Acknowledgment

This work was supported by the Laboratory of Electrical Engineering and Renewable Energy (LGEER), Faculty of Technology, Hassiba Benbouali University of Chlef.

### Credit Author Statement

Author Contributions: Chenoui Mohamed: Conceptualization, Methodology, Investigation, Software, Data Curation, Writing Original Draft Preparation, Visualization; Tebani Hocine: Supervision, Writing Review and Editing, Validation, Resources; Benyoucef Djilali: Co-supervision, Project Administration, Writing Review and Editing, Validation. All authors have read and agreed to the published version of the manuscript.

### References

- [1] Kabir, M., Habiba, U.E., Khan, W., Shah, A., Rahim, S., De Los Rios-Escalante, P. R., Farooqi, Z.-U.-R., Ali, L., Shafiq, M. (2023b). Climate change due to increasing concentration of carbon dioxide and its impacts on environment in 21st century; a mini review. *Journal of King Saud University - Science*, 35(5), 102693. DOI: 10.1016/j.jksus.2023.102693
- [2] Anwar, M.N., Iftikhar, M., Bakhat, B.K., Sohail, N.F., Baqar, M., Yasir, A., Nizami, A.S. (2019b). Sources of carbon dioxide and environmental issues. In *Sustainable Agriculture Reviews* (pp. 13–36). DOI: 10.1007/978-3-030-29298-0\_2
- [3] Florides, G.A., Christodoulides, P. (2008b). Global warming and carbon dioxide through sciences. *Environment International*, 35(2), 390–401. DOI: 10.1016/j.envint.2008.07.007
- [4] Centi, G., Quadrelli, E.A., Perathoner, S. (2013). Catalysis for CO<sub>2</sub> conversion: a key technology for rapid introduction of renewable energy in the value chain of chemical industries. *Energy & Environmental Science*, 6(6), 1711. DOI: 10.1039/c3ee00056g
- [5] Snoeckx, R., Bogaerts, A. (2017). Plasma technology – a novel solution for CO<sub>2</sub> conversion. *Chemical Society Reviews*, 46(19), 5805–5863. DOI: 10.1039/c6cs00066e
- [6] Sun, X., Bao, J., Li, K., Argyle, M.D., Tan, G., Adidharma, H., Zhang, K., Fan, M., Ning, P. (2020). Advance in using plasma technology for modification or fabrication of Carbon-Based materials and their applications in environmental, material, and energy fields. *Advanced Functional Materials*, 31(7). DOI: 10.1002/adfm.202006287
- [7] Bogaerts, A., Berthelot, A., Heijkers, S., Kolev, S., Snoeckx, R., Sun, S., Trenchev, G., Van Laer, K., Wang, W. (2017). CO<sub>2</sub> conversion by plasma technology: insights from modeling the plasma chemistry and plasma reactor design. *Plasma Sources Science and Technology*, 26(6), 063001. DOI: 10.1088/1361-6595/aa6ada
- [8] Ollegott, K., Wirth, P., Oberste-Beulmann, C., Awakowicz, P., Muhler, M. (2020). Fundamental properties and applications of dielectric barrier discharges in Plasma-Catalytic processes at atmospheric Pressure. *Chemie Ingenieur Technik*, 92(10), 1542–1558. DOI: 10.1002/cite.202000075
- [9] Brandenburg, R. (2018). Corrigendum: Dielectric barrier discharges: progress on plasma sources and on the understanding of regimes and single filaments (2017 Plasma Sources Sci. Technol. 26 053001). *Plasma Sources Science and Technology*, 27(7), 079501. DOI: 10.1088/1361-6595/aaced9
- [10] Xu, Y., Gao, Y., Dou, L., Xi, D., Qi, C., Lu, B., Shao, T. (2025). Low-temperature plasma-enabled CO<sub>2</sub> dissociation: a critical analysis of plasma setups and conversion mechanisms toward scale-up valorization. *Green Chemistry*. DOI: 10.1039/d5gc02037a
- [11] Aerts, R., Somers, W., Bogaerts, A. (2015). Carbon dioxide splitting in a dielectric barrier discharge plasma: A combined experimental and computational study. *ChemSusChem*, 8(4), 702–716. DOI: 10.1002/cssc.201402818
- [12] Nouri, E., Kardan, A., Mottaghitlab, V. (2024). Plasma reactors. In *Advances in Chemical and Materials Engineering Book Series* (pp. 1–33). DOI: 10.4018/979-8-3693-0904-9.ch001
- [13] Kozák, T., Bogaerts, A. (2014). Splitting of CO<sub>2</sub> by vibrational excitation in non-equilibrium plasmas: a reaction kinetics model. *Plasma Sources Science and Technology*, 23(4), 045004. DOI: 10.1088/0963-0252/23/4/045004
- [14] Paulussen, S., Verheyde, B., Tu, X., De Bie, C., Martens, T., Petrovic, D., ... Sels, B. (2010). Conversion of carbon dioxide to value-added chemicals in atmospheric pressure dielectric barrier discharges. *Plasma Sources Science and Technology*, 19(3), 034015. DOI: 10.1088/0963-0252/19/3/034015

- [15] Paulussen, S., Verheyde, B., Tu, X., De Bie, C., Martens, T., Petrovic, D., Bogaerts, A., Sels, B. (2010b). Conversion of carbon dioxide to value-added chemicals in atmospheric pressure dielectric barrier discharges. *Plasma Sources Science and Technology*, 19(3), 034015. DOI: 10.1088/0963-0252/19/3/034015
- [16] Ramakers, M., Michielsen, I., Aerts, R., Meynen, V., Bogaerts, A. (2015). Effect of argon or helium on the CO<sub>2</sub> conversion in a dielectric barrier discharge. *Plasma Processes and Polymers*, 12(8), 755–763. DOI: 10.1002/ppap.201400213
- [17] Budde, M., Engeln, R. (2024). Influence of energy transfer processes on the rovibrational characteristics of CO<sub>2</sub> in low-temperature conversion plasma with Ar and He admixture. *The Journal of Chemical Physics*, 160(24). DOI: 10.1063/5.0213892
- [18] Barkhordari, A., Karimian, S., Shahsavari, S., Krawczyk, D., Rodero, A. (2024). Influence of the argon admixture on the reactive oxide species formation inside an atmospheric pressure oxygen plasma jet. *Scientific Reports*, 14(1). DOI: 10.1038/s41598-024-54111-y
- [19] Vialetto, L. (2021). Modelling of plasma for CO<sub>2</sub> conversion: electron kinetics, chemistry and transport. [Phd Thesis 1 (Research TU/e / Graduation TU/e), Applied Physics and Science Education]. Eindhoven University of Technology.
- [20] Kowalski, T.Z. (2020). Analytical approach and calculation of gas gain in Ar-CO<sub>2</sub> mixture. *Journal of Instrumentation*, 15(07), P07008. DOI: 10.1088/1748-0221/15/07/p07008
- [21] Encarnação, P.M.C.C., Cortez, A.F.V., Pinto, M.G.A., Neves, P.N.B., Trindade, A.M.F., Escada, J., ... Conde, C.A.N. (2015). Experimental ion mobility measurements in Ar-CO<sub>2</sub> mixtures. *Journal of Instrumentation*, 10(01), P01010. DOI: 10.1088/1748-0221/10/01/p01010.
- [22] Talviste, R., Reino, C. R., Paris, P., Raud, J., Plank, T., Jögi, I. (2023b). Study of apparent effective ionization coefficient in CO<sub>2</sub> and Ar gas mixtures. *Physics of Plasmas*, 30(11). DOI: 10.1063/5.0160974
- [23] Hasan, M.I., Walsh, J.L. (2016). Numerical investigation of the spatiotemporal distribution of chemical species in an atmospheric surface barrier-discharge. *Journal of Applied Physics*, 119(20). DOI: 10.1063/1.4952574.
- [24] Grosch, H., Hoder, T., Weltmann, K.-d., Brandenburg, R. (2010). Spatio-temporal development of microdischarges in a surface barrier discharge arrangement in air at atmospheric pressure. *The European Physical Journal D*, 60(3), 547–553. DOI: 10.1140/epjd/e2010-00239-8.
- [25] Liao, Y., Zhong, W., Qian, M., Liu, S., Zhang, J., Wang, D. (2020). Numerical study on the reaction mechanism of CO<sub>2</sub> hydrogenation in atmospheric-pressure dielectric barrier discharge. *Journal of Applied Physics*, 128(23). DOI: 10.1063/5.0028174
- [26] Kim, H.C., Iza, F., Yang, S.S., Radmilović-Radjenović, M., Lee, J.K. (2005). Particle and fluid simulations of low-temperature plasma discharges: benchmarks and kinetic effects. *Journal of Physics D Applied Physics*, 38(19), R283–R301. DOI: 10.1088/0022-3727/38/19/r01
- [27] Bajon, C., Dap, S., Belinger, A., Guaitella, O., Hoder, T., Naudé, N. (2023b). Homogeneous dielectric barrier discharge in CO<sub>2</sub>. *Plasma Sources Science and Technology*, 32(4), 045012. DOI: 10.1088/1361-6595/acc9d9
- [28] Sohbatzadeh, F., Soltani, H. (2018). Time-dependent one-dimensional simulation of atmospheric dielectric barrier discharge in N<sub>2</sub>/O<sub>2</sub>/H<sub>2</sub>O using COMSOL Multiphysics. *Journal of Theoretical and Applied Physics*, 12(1), 53–63. DOI: 10.1007/s40094-018-0281-4
- [29] Amine, N.Y.M., Mohamed, M., Djilali, B. (2025). Investigation of AR/CH<sub>4</sub> mixtures in dielectric barrier discharge: A simulation approach for hydrogen production. *Bulletin of Chemical Reaction Engineering and Catalysis*, 20(3), 458–470. DOI: 10.9767/bcrec.20352
- [30] Zhang, Y.-T., Gao, S.-H., Zhu, Y.-Y. (2023). Efficient numerical simulation on dielectric barrier discharges at atmospheric pressure integrated by deep neural network. *Journal of Applied Physics*, 133(5). DOI: 10.1063/5.0136336
- [31] Elaissi, S., Alsaif, N.A.M. (2023). Modelling of nonthermal dielectric barrier discharge plasma at atmospheric pressure and role of produced reactive species in surface polymer microbial purification. *Polymers*, 15(5), 1235. DOI: 10.3390/polym15051235
- [32] Cortez, André. "A Practical Approach to Ion Mobility." *New Horizons in Time Projection Chambers*, Santiago de Compostela (Spain) (2020).
- [33] LXCAT, Electron Scattering Database, University of Toulouse, France. www.lxcat.net. retrieved on January 23, 2025.
- [34] Moss, M.S., Yanallah, K., Allen, R.W.K., Pontiga, F. (2017b). An investigation of CO<sub>2</sub> splitting using nanosecond pulsed corona discharge: effect of argon addition on CO<sub>2</sub> conversion and energy efficiency. *Plasma Sources Science and Technology*, 26(3), 035009. DOI: 10.1088/1361-6595/aa5b1d
- [35] Elahi, R., Simasiku, E.M., Trelles, J.P. (2023b). Computational modeling of CO<sub>2</sub> conversion by a solar-enhanced microwave plasma reactor. *Plasma Sources Science and Technology*, 32(6), 065018. DOI: 10.1088/1361-6595/acde08

- [36] Brezmes, A.O., Breilkopf, C. (2019b). Numerical analysis of atmospheric pressure plasma produced by a dielectric barrier discharge in a mixture of AR/CO<sub>2</sub>. *IEEE Transactions on Radiation and Plasma Medical Sciences*, 4(4), 498–511. DOI: 10.1109/trpms.2019.2961261
- [37] Beuthe, T.G.B.T.G., Chang, J.-S.C.J.-S. (1997). Chemical kinetic modelling of Non-Equilibrium AR-CO<sub>2</sub> thermal plasmas. *Japanese Journal of Applied Physics*, 36(7S), 4997. DOI: 10.1143/jjap.36.4997
- [38] Vermeiren, Vincent. Chemical kinetics modeling of non-equilibrium and thermal effects in vibrationally active CO<sub>2</sub> plasmas. Dissertation. University of Antwerp, 2020. <https://hdl.handle.net/10067/1733850151162165141>
- [39] Saidia, L., Belasri, A., Baadj, S., Harrache, Z. (2019). Physico-chemical investigation of pulsed discharge in CO<sub>2</sub>/O<sub>2</sub> gas mixture. *Plasma Physics Reports*, 45(5), 501–516. DOI: 10.1134/S1063780X1905009X.